Draft version May 22, 2019
Typeset using LaTeX **twocolumn** style in AASTeX62

Entrainment of low Mach number thermals in stratified domains

Evan H. Anders,[1,2] Daniel Lecoanet,[3,4] and Benjamin P. Brown[1,2]

[1] *Dept. Astrophysical & Planetary Sciences, University of Colorado – Boulder, Boulder, CO 80309, USA*
[2] *Laboratory for Atmospheric and Space Physics, Boulder, CO 80303, USA*
[3] *Princeton Center for Theoretical Science, Princeton, NJ 08544, USA*
[4] *Department of Astrophysical Sciences, Princeton, NJ 08544, USA*

(Received May 22, 2019; Revised ??; Accepted ??)

Submitted to ApJ

ABSTRACT

"Entropy rain," or the downard propagation of low entropy fluid, has been hypothesized as a dominant mechanism for carrying the solar luminosity in light of the recent Solar Convective Conundrum. One possible dynamical manifestation of these "raindrops" is that of dense, propagating vortex rings, referred to as "thermals" in the context of Earth's atmosphere. In this work, we develop an analytical theory describing entrainment in dense, antibuoyant vortex rings in stratified atmospheres. We show that this theory describes the evolution of laminar, axisymmetric thermals in highly stratified atmospheres and into the boussinesq limit. We discuss what the evolution of these thermals implies for the entropy rain hypothesis.

Keywords: hydrodynamics — turbulence — entrainment

1. INTRODUCTION

Recent observations of solar convection have revealed a convective conundrum. Power spectra have revealed weaker flows than anticipated at large length scales (Hanasoge et al. 2012; Greer et al. 2015), calling into question the existence of so-called "giant cells" driven by deep convection which would manifest as powerful, large-scale motions at the solar surface. This discrepancy between theory and observations has called into question our fundamental understanding of convection, sparking numerous targeted investigations the nature of convection in the Sun (Featherstone & Hindman 2016; O'Mara et al. 2016; Cossette & Rast 2016; Käpylä et al. 2017; Hotta 2017).

Spruit (1997) hypothesized that convective motions may be driven entirely by cool downflows at the surface of the Sun, and Brandenburg (2016) expanded upon this "entropy rain" hypothesis. Brandenburg's work includes a careful expansion of mixing length theory to incorporate flux contributions from nonlocal convective motions, and handles this theory in a horizontally-averaged sense. He includes some discussion of possible flow morphologies which could be manifestations of this entropy rain, and even includes some brief simulations of propogating Hill vortices. However, these simulations and discussions did not include include a fundamental piece of entropy rain: it is buoyant, and has an entropy deviation from the background atmosphere.

If entropy rain does evolve into downward propagating, dense, anti-buoyant vortex rings, it is important to understand how the filling factor of these basic convective elements is affected by their entropy signature. In the context of Earth's atmosphere, "thermals," or buoyant fluid regions which evolve into rising vortex rings, are thought to be the nucleus of cloud formation. While atmospheric, cloud-forming thermals always rise, the term is also used for the reverse, falling process and the evolution of thermals in the Boussinesq limit have been well studied in the laboratory for decades (see e.g. Morton et al. 1956; Scorer 1957), and more recently have been studied through Direct Numerical Simulation (DNS) in the laminar and turbulent regime (Lecoanet & Jeevanjee 2018). One fundamental result of these studies of thermals is that they experience a large degree of entrainment: their size expands with height and their propaga-

Corresponding author: Evan H. Anders
evan.anders@colorado.edu

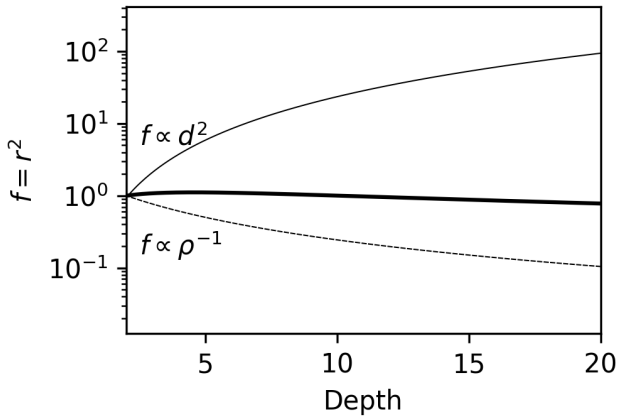

Figure 1. We have plotted the evolution of the filling factor, or radius squared, of a buoyant vortex ring with depth (the $n_\rho = 3$ case examined later in this work). Overplotted in a thin solid line is the prediction for filling factor growth in the Boussinesq case, and in the thin dashed line is plotted the prediction for pure horizontal compression, as in Brandenburg (2016).

tion velocity slows despite their buoyant nature. However, we do not know of a study in which the propagation of these thermals, and thus the nature of their entrainment, is affected by a significant atmospheric stratification.

In the absence of buoyantly-induced entrainment, Brandenburg (2016) suggests that the filling factor, f, of vortex rings should decrease like $f \propto \rho^{-1}$ for horizontal compression and $f \propto \rho^{-2/3}$ for spherical compression. On the other hand, the filling factor of Boussinesq thermals *increases* like $f \propto d^2$, where d is the depth propagated. These regimes are shown in Fig. 1, and compared to the true propagation of a thermal in an appreciably stratified environment.

In this work, we extend the study of Lecoanet & Jeevanjee (2018) to study the propagation of low-Mach number, cold thermals in stratified domains. We are specifically interested in how buoyant entrainment affects the scaling of the thermal radius, or filling factor, with depth. If buoyant entrainment is a dominant effect, it is possible that entropy rain would simply grow too large and stall before reaching the bottom of the solar convection zone. On the other hand, if the compression effects suggested by Brandenburg (2016) are the dominant effect, then it is possible that these thermals could propagate to the bottom of the solar convection zone, or potentially shrink to a sufficiently small size where thermal dissipation is significant.

In section 2, we develop a theoretical description of thermals in a stratified domain. In section 3, we describe the experiments conducted in this work. In section 4, we compare the results of our experiments to the theory developed in section 2. Finally, in section 5, we discuss what our results imply for the entropy rain hypothesis.

2. THEORY

2.1. *Phenomenological description of thermal evolution*

We show pictorally the evolution of cold thermalss from rest in Fig. 2 for two different domains which span a different number of density scale heights (n_ρ). In Fig. 2a, the evolution of a thermal in a weakly stratified domain with $n_\rho = 0.5$ density scale heights is shown. In Fig. 2b, the evolution of a thermal in an appreciably stratified domain with $n_\rho = 3$ density scale heights is shown. In both cases, the thermal's initial conditions are spherical, dense, low entropy perturbations of equal magnitude whose diameters are 5% of the domain depth. This dense sphere spins up into an axisymmetric vortex ring, and the vertical cross section through this vortex ring shows two circular vorticity & entropy minima. We find that the $n_\rho = 0.5$ case entrains and grows with depth, similarly to the Boussinesq regime. On the other hand, the $n_\rho = 3$ case has a radius which remains approximately constant over time. The goal of this paper is to understand the evolution of the thermal in the vortex ring stage. All of the thermals studied in this work are laminar, similar to the Hill vortices studied by Brandenburg (2016), but Lecoanet & Jeevanjee (2018) showed that laminar theory describes the evolution of turbulent thermals well. We reserve studies of turbulent thermals in stratified domains for future work.

In the following sections, we will use a description of the impulse and momentum of these thermals, as determined by their buoyant nature, to describe the evolution of their depth and radii with time.

2.2. *Evolution of momentum and impulse*

The evolution of thermals as buoyant vortex rings has been well described in the unstratified, Boussinesq limit for decades (see e.g. Lecoanet & Jeevanjee 2018, for a description and sources). Here we lay out a description of the momentum and impulse of the thermal which will later be used to describe thermal properties like radii and depth vs. time.

In this work, we study an ideal gas and focus on the ideal, low Mach number regime in an adiabatically stratified atmosphere. In this regime, a linearized equation of state describes the thermodynamics well, and the fully compressible Euler momentum equation takes the form (Brown et al. 2012),

$$\frac{\partial \boldsymbol{u}}{\partial t} + \boldsymbol{u} \cdot \nabla \boldsymbol{u} = -\nabla \varpi - \frac{S_1}{c_P} \boldsymbol{g}, \tag{1}$$

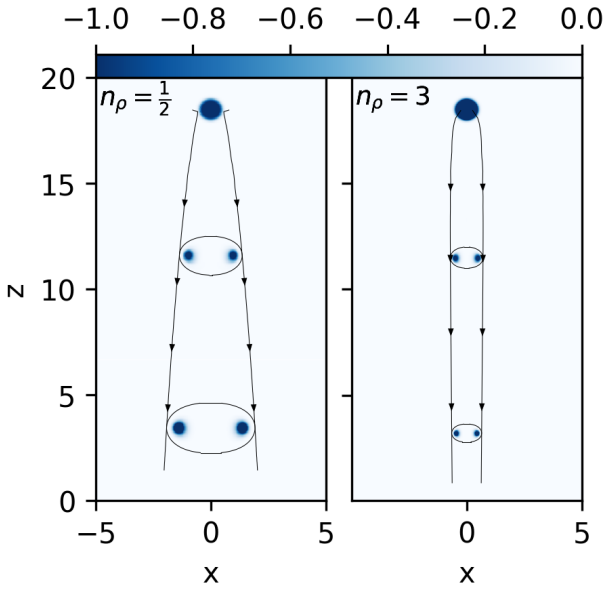

Figure 2. The evolution of $\rho S_1 r^3$, the mass-weighted entropy scaled by the thermal volume, is shown for two thermals. On the left is a thermal in a weakly stratified domain with $n_\rho = 1/2$ density scale heights and on the right is a thermal in a strongly stratified domain with $n_\rho = 3$. While both start with precisely the same initial condition, the case with low stratification expands with depth like the boussinesq case, whereas the strongly stratified thermal compresses with depth.

where $\boldsymbol{u}$ is the velocity, $\varpi = P_1/\rho_0$ is the reduced pressure, $S = c_V \ln T - R \ln \rho$ is the specific entropy, and thermodynamics are broken down into background (subscript 0) and fluctuating (subscript 1) components. In this work we find it instructive to examine the full momentum, and so multiplying this equation by the density, we obtain,

$$\frac{\partial(\rho \boldsymbol{u})}{\partial t} + \boldsymbol{u} \cdot \nabla(\rho \boldsymbol{u}) + \rho \boldsymbol{u}(\nabla \cdot \boldsymbol{u}) = -\rho \nabla \varpi - \rho \frac{S_1}{c_P} \boldsymbol{g}. \quad (2)$$

Hereafter we will define the total derivative, $D/Dt \equiv \partial/\partial t + \boldsymbol{u} \cdot \nabla$, and we acknowledge that the Langrangian derivative commutes with a volume integral such that

$$\frac{d}{dt} \int_{\mathcal{V}} f dV = \int_{\mathcal{V}} \left[\frac{Df}{Dt} + f(\nabla \cdot \boldsymbol{u}) \right] dV,$$

assuming that the volume $\mathcal{V}$ is advected with the fluid. Volume-integrating Eqn. 2, we thus find

$$\frac{d\boldsymbol{M}}{dt} = \int_{\mathcal{V}} \left(-\rho \nabla \varpi - \rho \frac{S_1}{c_P} \boldsymbol{g} \right) dV, \quad (3)$$

where the volume-integrated momentum is defined $\boldsymbol{M} \equiv \int_{\mathcal{V}} \rho \boldsymbol{u} dV$. At this point we will make the assumption of a plane-parallel atmosphere in which the gravity is constant, $\boldsymbol{g} = -g\hat{z}$, and note that the z-component of the volume-integrated momentum evolves according to

$$\frac{dM_z}{dt} = \int_{\mathcal{V}} \left(-\rho \frac{\partial \varpi}{\partial z} + \rho g \frac{S_1}{c_P} \right) dV. \quad (4)$$

At this point, we find it useful to define the total buoyancy,

$$B \equiv \int_{\mathcal{V}} \rho \, S_1 \, \frac{g}{c_P} \, dV, \quad (5)$$

as in the absence of viscosity and detrainment, this is a conserved quantity during thermal evolution (REFERENCE FIGURE). Furthermore, in the Boussinesq limit, the work of Tarshish et al. (2018) shows that pressure terms reduce the efficacy of the buoyancy in changing the momentum by effectively reducing the buoyant acceleration by some factor $\beta \sim 0.5$. As a result, we can approximate the growth of a thermal's momentum according to

$$\frac{dM_z}{dt} \approx \beta B. \quad (6)$$

After describing the growth of the thermal's integrated momentum with time, we turn our attention to the hydrodynamic impulse, which in the stratified limit is defined (Shivamoggi 2010),

$$\boldsymbol{I} = \frac{1}{2} \int_{\mathcal{V}} \boldsymbol{x} \times (\nabla \times (\rho \boldsymbol{u})) dV, \quad (7)$$

where $\boldsymbol{x}$ is the position vector. Impulse is equivalent to the time-integrated work acting on the fluid resulting in the current fluid motion. Per Shivamoggi (2010), changes in the impulse can be expressed as

$$\frac{d\boldsymbol{I}}{dt} = \int_{\mathcal{V}} \frac{\partial(\rho \boldsymbol{u})}{\partial t} dV = B\hat{z} - \int_{\mathcal{V}} \left[\rho \nabla \varpi + \nabla \cdot (\rho \boldsymbol{u} \boldsymbol{u}) \right] dV,$$

where, importantly, the *eulerian* time derivative of the momentum is inside of the volume integral here. Under the proper specification of boundary conditions, the integral term is zero, and the vertical impulse of a thermal thus straightforwardly changes in time as

$$\frac{dI_z}{dt} = B. \quad (8)$$

We have thus retrieved the two findings on which our theory of thermal evolution will be built: *both the impulse and momentum experience constant changes in time determined by the buoyant nature of the thermal.*

In the low-Mach number limit in which changes in density from the background are negligible, and in the limit of a thin-core vortex ring, the impulse of a vortex ring can be approximated as

$$I_z \approx \pi \rho r^2 \Gamma, \quad (9)$$

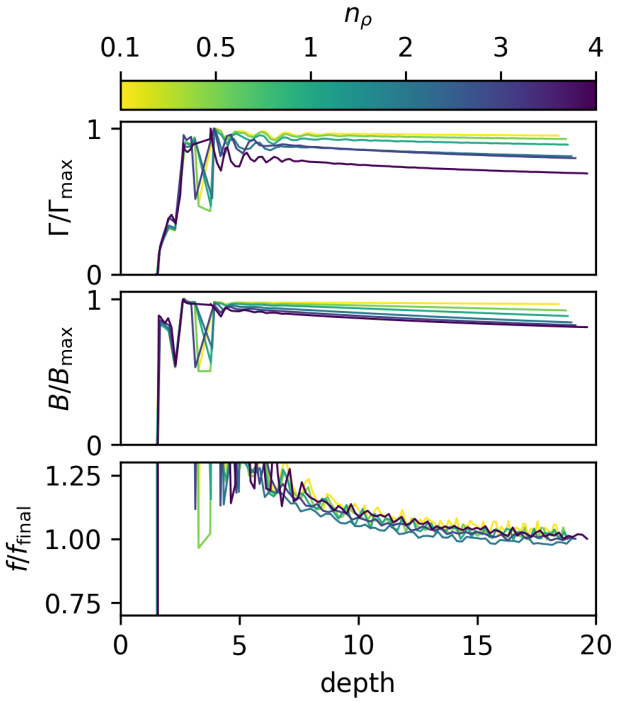

Figure 3. Plotted are time traces for three quantities which we assume to be constant in our thermal theory. In (a) and (b), the circulation and buoyancy, divided by their maxima, are plotted vs. depth. We see that with increasing stratification, there is marginally more detrainment of both of these quantities, but to first order they are constant over the evolution of the thermal. In (c) the constant $f = V/r^3$ is plotted; after significant noise during the development of the vortex ring, this quantity remains relatively constant, and increasingly approaches a constant with depth.

where r is the radius of the thermal from its axis of symmetry to the maxima of its buoyant signature, and $\Gamma = \int_{\mathcal{A}} (\nabla \times \boldsymbol{u}) dA$ is the integrated circulation in a cross-section of the vortex ring. Through integration of the momentum equation, it can be shown that in the absence of viscous effects, changes in circulation in an axisymmetric vortex ring are

$$\frac{d\Gamma}{dt} = \oint_{\mathcal{C}} g \frac{S_1}{c_P} \hat{z} \cdot d\boldsymbol{x}, \tag{10}$$

where $\mathcal{C}$ is the contour around the area $\mathcal{A}$ in which the circulation is contained and $d\boldsymbol{x}$ is the line integral element around that contour. For the case of a vortex core in which the entropic signature is contained tightly in the core, as in Fig. 2, any contour which is drawn around the vortex core should conserve circulation in the absence of viscosity.

2.3. *Parameterized description of thermal evolution*

After spinning up, we assume that the thermal is characterized by a constant buoyant signature, B_0, and constant circulation, Γ_0. While these thermals began as initial spherical perturbations, they can be modeled as vortex rings which evolved from a "virtual origin" at which they had no radius. From this virtual origin, the vortex ring's momentum and impulse grow to a value of M_0 and I_0 at time $t = 0$ when the true thermal is released from rest.

We first note, as in Fig. 3a, that the buoyancy in our thermals is not necessarily perfectly constant in time, and that effects like detrainment result in a minor reduction of the buoyant signature of our thermals. We thus express the buoyancy as

$$B \approx \chi B_0, \tag{11}$$

where χ is a constant of O(1) which represents this detrainment. We then integrate Eqn. 8 in time,

$$I_z = \chi B_0 t + I_0.$$

Following Eqn. 10, we take Γ_0 to be constant, which is a decent assumption in our numerical experiments, see Fig. 3b. Combining Eqns. 3 and 9, we retrieve our first result,

$$r = \sqrt{\frac{\chi B_0 t + I_0}{\pi \rho \Gamma_0}}. \tag{12}$$

In the Boussinesq limit where $\rho \to$ constant, we retrieve the $r \propto \sqrt{t}$ scaling found in the Boussinesq regime by Lecoanet & Jeevanjee (2018). We find that the inclusion of stratification adds the additional complexity of $r \propto \rho^{-1/2}$, such that downward-propogating vortex rings (as studied here) will entrain less than boussinesq thermals, and upward-propogating rings will entrain more. In the absence of buoyancy ($B = 0$), this result aligns with the prediction for purely horizontal compression noted by Brandenburg (2016) of $r^2 \propto \rho^{-1}$.

The momentum can likewise be integrated like the impulse,

$$M_z = \beta \chi B_0 t + M_0.$$

For the proper choice of vertical velocity, $w_{\rm th}$, and volume, $\mathcal{V}$, the momentum can be expressed precisely as

$$M_z = \rho \mathcal{V} w_{\rm th},$$

and the volume can be approximated as $\mathcal{V} = f r^3$, where f is a parameter which we take to be constant. This assumption is perhaps not as perfect as the assumptions of constant B_0 or Γ_0 (see Fig. 3c), but it is nevertheless not a bad assumption. Combining our approximate expressions, and inserting our theoretical description of r

(Eqn. 12), we retrieve

$$\rho^{-1/2} w_{\rm th} = \left(\frac{(\pi\Gamma)^{3/2}}{f}\right) \frac{\beta\chi B_0 t + M_0}{(\chi B_0 t + I_0)^{3/2}}. \quad (13)$$

Defining the thermal velocity $w_{\rm th} \equiv dz_{\rm th}/dt$, and making the assumption that the vortex ring starts at a "virtual origin" (CITE) at $t = 0$ where it has no impulse or momentum ($I_0 = M_0 = 0$), an integrable expression for the evolution of thermal position over time can be retrieved,

$$\frac{dz_{\rm th}}{\rho(z_{\rm th})^{1/2}} = \left(\frac{\beta(\pi\Gamma)^{3/2}}{f(\chi B_0)^{1/2}}\right) \frac{dt}{t^{1/2}} \quad (14)$$

If the atmospheric stratification in which the thermal is falling is known, this result can be integrated with $\rho(z_{\rm th})$ plugged in in order to find the position of the thermal as a function of time. We leave this result general for now, and will integrate it using the polytropic stratification used in our simulations at the end of section 3.

2.4. *Solution for thermal evolution in a Polytrope*

Throughout this work we will study a polytrope, as is specified later in Eqn. 21. Integrating Eqn. 14 with this specific density stratification, we find

$$z_{\rm th} = \nabla_{\rm ad}^{-1}\left[\left(\frac{2C}{\alpha}\sqrt{t + t_{\rm off}} + T_0^{1/\alpha}\right)^{\alpha} - 1\right] + L_z, \quad (15)$$

where $C \equiv \beta\pi^{3/2}\nabla_{\rm ad}/f\sqrt{\Gamma^3/(\chi B)}$, the temperature at the virtual origin is $T_0 = 1 + \nabla_{\rm ad}(z_0 - L_z)$, $\alpha^{-1} = 1 - m_{\rm ad}/2$, and assuming that the polytropic index is $m_{\rm ad} < 2$ (which is valid for our case of $m_{\rm ad} = 1.5$ studied here). In the limit of large stratification, we thus find that $z_{\rm th} \propto t^2$ for our case of $\alpha = 4$.

The thermal is initialized as a uniform sphere of dense fluid, and it quickly spins up into a vortex ring. While we do not attempt to model the spin-up phase in this paper, it can be parameterized by the buoyancy B_0, circulation Γ, as well as the virtual origin z_0, and temporal offset t_off which are the height and time a which the vortex ring would have had zero radius in the absence of a spin-up phase. Our theory also involves the volumetric aspect ratio of the thermal f, the detrainment fraction χ, and the effective buoyancy β. These appear to be constant or only weakly dependent on the stratification for the thermals we have simulated.

3. EXPERIMENT

3.1. *Anelastic Simulations*

In this work, we primarily study the evolution of 2D, azimuthally symmetric, anelastic thermals in cylindrical coordinates. We later verify that select simulations produce the same results as 3D fully compressible simulations in cartesian domains (see sec. REF). The LBR anelastic equations are (Lecoanet et al. 2014),

$$\nabla \cdot \boldsymbol{u} = -w\partial_z \ln \rho_0, \quad (16)$$

$$\partial_t \boldsymbol{u} + \boldsymbol{u}\cdot\nabla\boldsymbol{u} = -\nabla\varpi + S_1\hat{z} + \frac{1}{\rho_0 {\rm Re}}\left[\nabla^2\boldsymbol{u} + \frac{1}{3}\nabla(\nabla\cdot\boldsymbol{u})\right] \quad (17)$$

$$\partial_t S_1 + \boldsymbol{u}\cdot\nabla S_1 = \frac{1}{\rm Re}\left(\frac{1}{{\rm Pr}\rho_0 c_P}\left[\nabla^2 S_1 + \partial_z \ln T_0 \cdot \partial_z S_1\right] + \frac{-(\nabla_{\rm ad})}{\rho_0 T_0}\sigma_{ij}\partial_{x_i} u_j\right), \quad (18)$$

where $\nabla_{\rm ad} \equiv g(e^{n_\rho/m_{\rm ad}} - 1)/(L_z c_P)$ and $\bar{\bar{\boldsymbol{\sigma}}}$ is the viscous stress tensor in units of inverse time. In our azimuthally symetric domain, we assume that $\partial_\phi = 0$; as the initial conditions of our simulations are at rest and have no azimuthal velocity, u_ϕ, we explicitly impose that $u_\phi = 0$; therefore $\boldsymbol{u} = u_r\hat{r} + w\hat{z}$.

These equations have been nondimensionalized in the same manner as in Lecoanet & Jeevanjee (2018) such that the length scale is the diameter of the initial thermal perturbation and the velocity scale is the freefall velocity. The timescale is thus the freefall crossing time of this unit length. These atmospheres are fully specific in terms of the Reynolds number and Prandtl number,

$${\rm Re} = \frac{u_{th}L_{th}}{\nu}, \qquad {\rm Pr} = \frac{u_{th}L_{th}}{\chi}, \qquad u_{th}^2 = \frac{gL_{th}\Delta s}{c_P}, \quad (19)$$

where u_{th} is the freefall velocity, L_{th} is the thermal length scale, and Δs is the magnitude of the specific entropy signature of the thermal.

We choose an atmospheric model in which the dynamic viscosity, $\mu = \rho_0\nu$, and the thermal conductivity, $\kappa = \rho_0\chi$, are both uniform and constant in time. The diffusivities ν and χ therefore scale inversely with the density. As the diffusivities scale with depth, Re is specified at the thermal's initial depth. All simulations conducted in this work use a value of ${\rm Re} = 600$ and ${\rm Pr} = 1$.

3.2. *Atmosphere & Initial conditions*

We study an ideal gas whose equation of state is $P = \rho T$ and whose stratification is a perfectly adiabatic polytrope,

$$T_0 = 1 + (\nabla_{\rm ad})(z - L_z) \quad (20)$$

$$\rho_0 = T_0^{m_{\rm ad}}, \quad (21)$$

where $m_{\rm ad} = (\gamma - 1)^{-1}$, and the adiabatic temperature gradient in these nondimensional atmospheres is

set with $g = m_{\rm ad}+1$ and $\tilde{L}_{\rm th} = (e^{n_\rho/m_{\rm ad}}-1)/L_z$, where n_ρ is the number of density scale heights spanned by the atmosphere and $L_z = 20$ is the nondimensional depth of the atmosphere in units of thermal diameters.

To initialize the simulation, we specify a spherical initial specific entropy perturbation,

$$S_1 = -\frac{A}{2}\left[1 - \mathrm{erf}\left(\frac{r' - r_{th}}{\delta}\right)\right], \tag{22}$$

where $A = 1$ for our scaled equations. Here, $r' = \sqrt{r^2 + (z-z_0)^2}$, where $z_0 = L_z - 3r_{\rm th}$, with the thermal radius set as $r_{th} = 0.5$, and a smoothing width, $\delta = 0.1$.

3.3. *Fully Compressible Simulations*

In order to verify the validity of our 2D Anelastic simulations, we evolve select thermals according to the 3D Navier Stokes equations in a cartesian domain. We use the $(T, \ln\rho)$ formulation of the equations in which we have previously studied fully compressible convection at low and high Mach number (Lecoanet et al. 2014; Anders & Brown 2017),

$$\frac{\partial \ln\rho_1}{\partial t} + \epsilon^{-1}\left(\boldsymbol{u}\cdot\nabla\ln\rho_0 + \nabla\cdot\boldsymbol{u}\right) = -\boldsymbol{u}\cdot\nabla\ln\rho_1, \tag{23}$$

$$\frac{\partial \boldsymbol{u}}{\partial t} + \nabla T_1 + T_1\nabla\ln\rho_0 + T_0\nabla\ln\rho_1 = -\epsilon T_1\nabla\ln\rho_1 + \frac{1}{\rho\mathrm{Re}}\left[\nabla^2\boldsymbol{u} + \frac{1}{3}\nabla(\nabla\cdot\boldsymbol{u})\right] \tag{24}$$

$$\frac{\partial T_1}{\partial t} + \epsilon^{-1}\left[\boldsymbol{u}\cdot\nabla T_0 + (\gamma-1)T_0\nabla\cdot\boldsymbol{u}\right] = -\left[\boldsymbol{u}\cdot\nabla T_1 + (\gamma-1)T_1\nabla\cdot\boldsymbol{u}\right] + \frac{1}{\rho c_V\mathrm{Re}}\left[\frac{1}{\mathrm{Pr}}\nabla^2 T_1 + \sigma_{ij}\partial_{x_i}u_j\right]. \tag{25}$$

These equations have been nondimensionalized on the same length and timescales as the anelastic equations, use the same atmospheric profiles and assumptions, and we have explicitly assumed that the background atmosphere $(T_0, \ln\rho_0)$ is in hydrostatic and thermal equilibrium in the writing of these equations. The new parameter $\epsilon = u_{th}^2$ is the magnitude of entropy perturbations and sets the Mach number of the thermal flows, and we use $\epsilon = 10^{-4}$ in this work.

In setting the specific entropy to an equivalent condition to that specified in Eqn. 22, we note that it is essential that the initial perturbation be in pressure equilibrium. The set of initial conditions that achieves this is

$$\ln\rho_1 = S_1/c_P, \qquad T_1 = T_0(e^{-\ln\rho_1} - 1). \tag{26}$$

3.4. *Numerics*

We evolve our simulations forward in time using the Dedalus[1] pseudospectral framework (Burns et al. 2016) to time-evolve our equations. For our 2D simulations, we use using an implicit-explicit (IMEX), third-order, four-stage Runge-Kutta timestepping scheme RK443 (Ascher et al. 1997), and for our 3D simulations we use the second order semi-implicit backward differentiation formulation SBDF2 (Wang & Ruuth 2008).

Our 3D simulations are decomponsed on Fourier bases in the horizontal directions ($x, y \in [-L_r, L_r]$) and Chebyshev bases vertically ($z \in [0, L_z]$) with impenetrable, stress free, fixed-temperature boundary conditions at the upper and lower boundaries ($T_1 = w = \partial_z u = \partial_z v = 0$ at $z = [0, L_z]$). Our 2D simulations are decomposed on a Fourier ($z \in [0, L_z]$) and Chebyshev ($r \in [0, L_r]$) domain, with boundary conditions of $\partial_r S_1 = u_r = w = 0$ at $r = L_r$.

As a result of our theory being largely derived in the anelastic, axisymmetric limit, we have chosen to focus the bulk of our attention on our 2D, axisymmetric anelastic simulations. Furthermore, the 2D nature of these simulations allows us to much more feasibly study high density stratifications using fewer computational resources. The 3D fully compressible simulations serve primarily as a verification of the anelastic results in the low Mach number regime in which the anelastic constraint is not explicitly true, and in the 3D case where axisymmetry is not baked into the equations.

While natural processes are very turbulent, we have chosen to study the evolution of laminar thermals here. Lecoanet & Jeevanjee (2018) showed for an ensemble of laminar and turbulent thermals that the measured entrainment of the evolved vortex rings in the turbulent case is well described by laminar theory. As we are not aware of a developed laminar theory in the stratified regime in the literature, like the one developed here, we have restricted the simulations in this work to the laminar regime in order to test our new theory in the regime where it should be transparent to verify its validity.

4. RESULTS

The measured values of these parameters for the cases studied in this paper are presented in table 1.

In Fig. 4, we show the measured depth $d_{\rm th} = L_z - z_{\rm th}$ of the thermal as a function of time for low and high stratification. At very low stratification (e.g., $n_\rho = 0.1$), the thermal is small compared to the local density scale height at all depths, and it evolves roughly according to the Boussinesq prediction of $d \propto \sqrt{t}$. As the stratification increases, the thermal begins to transit the domain

[1] http://dedalus-project.org/

Table 1. Simulation output parameterization

n_ρ	T_0	$t_{\rm off}$	B	Γ	f	χ	β
2D Anelastic Simulations							
0.1	0.985	0.166	-0.547	-2.17	7.01	1.04	0.499
0.5	0.918	0.704	-0.568	-2.12	7.04	0.976	0.490
1	0.827	1.09	-0.601	-2.05	7.07	0.915	0.480
2	0.677	1.26	-0.712	-1.89	7.08	0.841	0.456
3	0.619	1.01	-0.946	-1.73	7.08	0.808	0.436
4	0.698	0.622	-1.47	-1.59	7.10	0.793	0.422
5							
3D Fully Compressible Simulations							
0.5	0.924	0.583	-0.568	-2.12	6.66	0.978	0.452
1	0.832	1.26	-0.601	-2.05	6.88	0.902	0.454
2	0.666	1.53	-0.711	-1.89	7.08	0.822	0.450

NOTE— Values from fully compressible simulations have been rescaled in post-processing for direct comparison with 2D anelastic cases

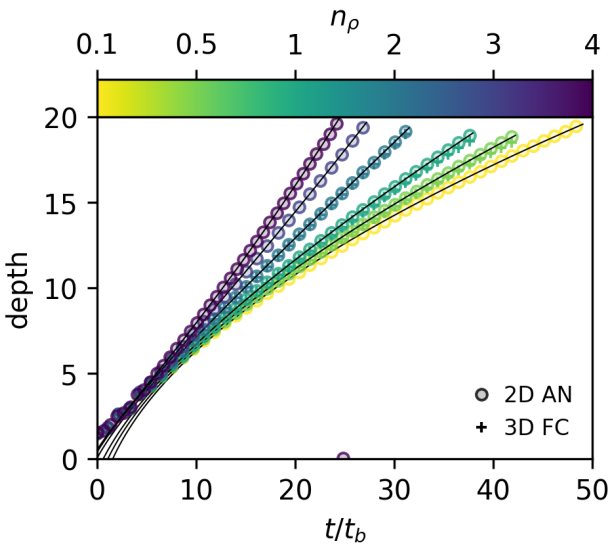

Figure 4. Shown are the measured depths of thermals as a function of time for all 2D Anelastic and 3D Fully compressible simulations conducted in this work. Overplotted is the theoretical prediction for depth as a function of time.

more quickly and approaches the limit of $d \propto t^2$ predicted in the highly stratified limit of Eqn. 15. The theoretical fits for depth from the prediction of Eqn. 15 are plotted over the measured data and show remarkable agreement.

In Fig. 5a, we plot the measured thermal radius vs. depth, with the theoretical predictions of Eqns. 12 & 15 plotted as lines over the data. In the low stratification limit, the radius of the thermal grows linearly with depth, $r \propto d$, aligning with the Boussinesq limit shown in Lecoanet & Jeevanjee (2018). This growth of the ther-

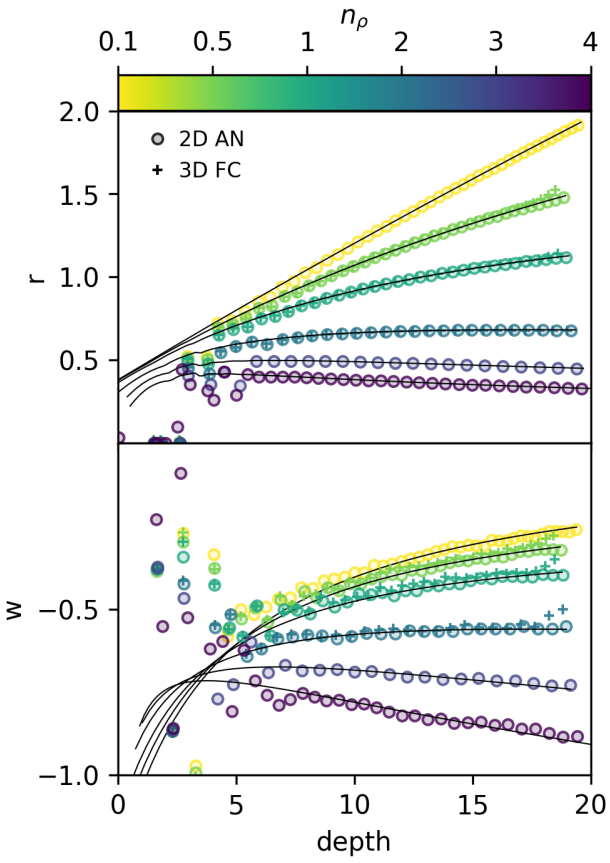

Figure 5. Shown are (a) the measured radii of thermals as a function of depth and (b) the measured thermal velocities as a function of depth for all 2D Anelastic and 3D Fully compressible simulations conducted in this work. Overplotted are the predictions from theory.

mal is the result of entrainment of environmental fluid and results an an accompany decceleration like $w \propto d^{-1}$ in the Boussinesq limit, as is shown in Fig. 5b. However, as stratification increases, the thermal entrains less environmental fluid and expands less, eventually even contracting with depth in the high-stratification limit. This lessened entrainment is, unsurprisingly, accompanied by greater acceleration of the thermal. As in the case of depth vs. time, the overplotted theoretical predictions show excellent agreement with the measured data.

These results suggest that there are two regimes of downflowing thermal behavior:

1. A low-stratification "stalling" regime, in which the thermal entrains environmental fluid and slows down, acting much like the Boussinesq regime, and

2. A high-stratification "falling" regime, in which the thermal falls fast enough that compression due to the atmospheric stratification results in minimal entrainment and the thermal accelerates as it falls deeper into the atmosphere.

4.1. *Verification of 2D Anelastic approximation*

In Fig. 6, we display in more detail a comparison of our 2D Anelastic and 3D Fully Compressible cases. In Fig. 6a, depth vs time is shown, and the fractional difference between FC and AN cases is shown in Fig. 6b. Differences between the two cases are $\leq 2\%$ for all times, with greater error towards the end of the simulations as the FC simulations begin to interact with the impenetrable boundary at the bottom of their simulation domains. In Fig. 6c, radius vs. depth is shown, and the fractional difference between FC and AN cases is shown in Fig. 6d. Aside from the very end of the simulation when the FC boundary conditions begin to matter, there is remarkable agreement between the two cases, with $< 1\%$ differences between the two cases after early times in which the thermal is still developing into a vortex ring.

This close agreement between low Mach number Fully Compressible simulations and Anelastic simulations parallels the agreement between the equation sets seen in Lecoanet et al. (2014), and gives us confidence in our anelastic results at higher levels of stratification, where the 2D simulations are much more numerically feasible than the 3D fully compressible simulations.

5. DISCUSSION

In this work we have extended the theory of the evolution of buoyant thermals into the low-Mach number, stratified regime and have shown that that theory has remarkable agreement with the results of both Anelastic and Fully compressible simulations.

However, we note that both the falling and stalling regimes observed here could result in interesting problems for the entropy rain hypothesis. If solar convection were comprised of thermals in the stalling regime, it is unlikely that such elements would ever make it to the base of the solar convection zone, stalling much closer to the solar surface and depositing their entropy signature there – possibly agreeing with the hypothesis of supergranulation as the largest buoyantly driven scale of solar motion. On the other hand, if solar convection is comprised of thermals in the falling regime, then it is possible that as these thermals compress and accelerate, diffusive effects and potentially viscous heating could become important. We discuss these possibilities further in section 5

We should have some discussion on these topics:

1. speculation about extensions to the solar regime. Do things on the sun shrink to the point where they viscously dissipate? Do they stall?

2. Talk about what would happen if we were to study up-thermals.

3. Extensions, and we trust that these results should hold in the regime of solar convection where things are turbulent.

This work was supported by NASA Headquarters under the NASA Earth and Space Science Fellowship Program – Grant 80NSSC18K1199. This work was additionally supported by NASA LWS grant number NNX16AC92G. Computations were conducted with support by the NASA High End Computing (HEC) Program through the NASA Advanced Supercomputing (NAS) Division at Ames Research Center on Pleiades with allocation GID s1647.

APPENDIX

A. THERMAL TRACKING

We use a thermal tracking algorithm very similar to the one used in Lecoanet & Jeevanjee (2018) and inspired by the work of Romps & Charn (2015).

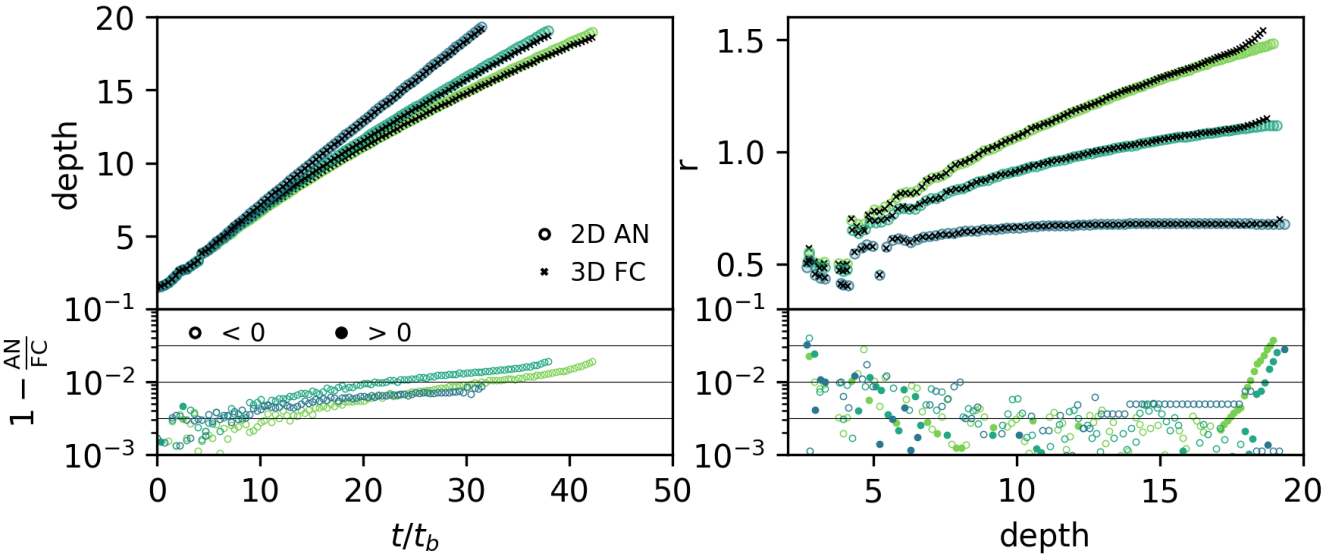

Figure 6. Measured values of (a) depth vs. time and (c) radius vs. depth are plotted for both the 2D anelastic and 3D fully compressible simulations. The fractional difference between anelastic and fully compressible results are respectively shown in (b) and (d).

Table 2. Table of simulation information

n_ρ	L_r	nr or nx = ny	nz	$t_{evolution}$	safety
2D Anelastic Simulations					
0.1	5	128	512	49	0.2
0.5	5	128	512	42.5	0.2
1	5	128	512	38	0.2
2	5	128	512	31.75	0.2
3	5	256	512	27.25	0.15
4	5	256	512	25	0.1
5	5	256	512	22.8	0.05
3D Fully Compressible Simulations					
0.5	5	256	512	42.5	0.8
1	4	256	512	38	0.8
2	3.5	256	1536	31.75	0.8

NOTE—

We begin by measuring the thermal's height versus time. To do so, we average the domain's entropy profile in radius and azimuth to create an average profile of entropy with height, and then assume that the thermal's vortex core is located at the entropy minima of each of those profiles. We numerically differentiate these found values of height vs. time using (insert numerical differentiation technique here) and then calculate the streamfunction of the velocity field as in Romps & Charn (2015),

$$\frac{\partial \psi}{\partial r} = 2\pi\rho r(w - w_{\rm th}), \tag{A1}$$

with the boundary condition that $\psi = 0$ at $r = 0$. The contour defined by $\psi = 0$ from this solution is taken to be the outline of the thermal, and the volume of the thermal is taken to be the volume radially inward from that contour.

B. TABLE OF SIMULATIONS

REFERENCES

Anders, E. H., & Brown, B. P. 2017, Physical Review Fluids, 2, 083501

Ascher, U. M., Ruuth, S. J., & Spiteri, R. J. 1997, Applied Numerical Mathematics, 25, 151

Brandenburg, A. 2016, ApJ, 832, 6

Brown, B. P., Vasil, G. M., & Zweibel, E. G. 2012, ApJ, 756, 109

Burns, K., Vasil, G., Oishi, J., Lecoanet, D., & Brown, B. 2016, Dedalus: Flexible framework for spectrally solving differential equations, Astrophysics Source Code Library, , , ascl:1603.015

Cossette, J.-F., & Rast, M. P. 2016, ApJ, 829, L17

Featherstone, N. A., & Hindman, B. W. 2016, ApJ, 830, L15

Greer, B. J., Hindman, B. W., Featherstone, N. A., & Toomre, J. 2015, ApJ, 803, L17

Hanasoge, S. M., Duvall, T. L., & Sreenivasan, K. R. 2012, Proceedings of the National Academy of Science, 109, 11928

Hotta, H. 2017, ApJ, 843, 52

Käpylä, P. J., Rheinhardt, M., Brand enburg, A., et al. 2017, ApJ, 845, L23

Lecoanet, D., Brown, B. P., Zweibel, E. G., et al. 2014, ApJ, 797, 94

Lecoanet, D., & Jeevanjee, N. 2018, arXiv e-prints, arXiv:1804.09326

Morton, B. R., Taylor, G., & Turner, J. S. 1956, Proceedings of the Royal Society of London Series A, 234, 1

O'Mara, B., Miesch, M. S., Featherstone, N. A., & Augustson, K. C. 2016, Advances in Space Research, 58, 1475

Romps, D. M., & Charn, A. B. 2015, Journal of Atmospheric Sciences, 72, 2890

Scorer, R. S. 1957, Journal of Fluid Mechanics, 2, 583

Shivamoggi, B. K. 2010, Physics Letters A, 374, 4736

Spruit, H. C. 1997, Mem. Soc. Astron. Italiana, 68, 397

Tarshish, N., Jeevanjee, N., & Lecoanet, D. 2018, Journal of Atmospheric Sciences, 75, 3233

Wang, D., & Ruuth, S. J. 2008, Journal of Computational Mathematics, 26, 838